Effect of shear-coupled grain boundary motion on coherent precipitation

M. Weikamp and R. Spatschek
Institute for Energy and Climate Research IEK-2, Forschungszentrum Jülich GmbH, 52425 Jülich, Germany

(Received 4 May 2019; published 6 August 2019)

We examine the interaction between precipitates and grain boundaries, which undergo shear-coupled motion. The elastic problem, emerging from grain boundary perturbations and an elastic mismatch strain induced by the precipitates, is analyzed. The resulting free elastic energy contains interaction terms, which are derived numerically via the integration of the elastic energy density. The interaction of the shear-coupled grain boundary and the coherent precipitates leads to potential elastic energy reductions. Such a decrease of the elastic energy has implications for the grain boundary shape and also for the solubility limit near the grain boundary. By energy minimization we are able to derive the grain boundary shape change analytically. We apply the results to the Fe-C system to predict the solubility limit change of cementite near an α-iron grain boundary.

DOI: 10.1103/PhysRevB.100.054103

I. INTRODUCTION

The understanding and the associated targeted influencing of mechanical properties of steels and alloys are an important and necessary aspect of materials science. The process of precipitation and, consequently, the presence of secondary phases with different properties are an important part of a microstructure. Cementite, for example, is very brittle but also hard and can reduce the effectiveness of an alloy or steel as it can act as a crack initiator [1]. Precipitates in general also influence dislocation movement and can therefore also strengthen the material (precipitation hardening [2]). In an earlier study [3] the precipitation of hydrides near surfaces was investigated, showing that elastic relaxation near free surfaces leads to significant differences concerning the phase stability compared to bulk precipitation. The interaction of precipitates and a free surface leads to a reduction of the elastic energy and therefore results in a change in the solubility limit. A transfer to interfaces was shown in Ref. [4], where a grain boundary was described as a mesoscopic layer with different elastic properties compared to the bulk. In this representation the grain boundary acts as a generally nonfree surface, and an influence on the solubility limit is observable. However, such an effective picture does not consider microscopic details of strengthening or stress release mechanisms. The aim of the present paper is therefore a more explicit consideration of stress release mechanisms due to morphological rearrangements of grain boundaries, in particular through shear-coupled motion, in conjunction with precipitate formation.

Shear-coupled motion of grain boundaries describes the normal motion of a grain boundary while the grains are sheared parallel to each other. This reversible interaction has been known for quite some time, first theoretically predicted by Read and Shockley in 1950 [5]. The authors derived that for low-angle symmetric tilt grain boundaries the collective movement of edge dislocations leads to the normal grain boundary motion as a response to shear stress. The first experimental evidence was found a few years later in zinc bicrystals [6,7]. The theoretical work of Cahn and Taylor [8] in 2004 led to a unified approach to describe the mechanism of pure sliding and shear-coupled motion. Molecular dynamics (MD) simulations on symmetrical [001] tilt boundaries revealed [9,10] that the underlying phenomenon is also applicable to high-angle grain boundaries, which cannot be considered an array of isolated dislocations. In Ref. [11] the shear-coupling behavior and misorientation angle dependence were investigated by phase field crystal simulations, showing also a transition from coupled motion to sliding at higher homologous temperatures. Further experimental [12] and numerical [13] studies showed that shear-coupled motion also occurs for more realistic and complex asymmetric grain boundaries. Another investigation [14] revealed that mixed-mode grain boundaries with a twist component also undergo shear-coupled motion correlated to the tilt fraction of the grain boundary. In Ref. [15] the $\Sigma5(310)$ grain boundary in Al was investigated by MD simulations. The interaction between shear and normal grain boundary motion has been observed, where the multiplicity of the grain boundary leads to different grain boundary structures after thermal relaxation. Another MD study [16] shed light on the different modes of dislocation movement of a [001] grain boundary in bcc W, coming to the conclusion that the $\langle 110 \rangle$ mode of the dislocation movement leads to easier shuffling of the atoms at the grain boundary. Further publications [17,18] investigated the interaction between shear-coupled grain boundary motion and a lamellar precipitate, which engulfs the boundary, as such an arrangement is energetically favorable. A linear stability analysis and phase field crystal simulations show that grain boundaries can become unstable and breakups occur. In Ref. [18] the authors also showed similar simulation results for a spherical inclusion. All of these studies demonstrate that any complex grain boundary structure can exhibit shear-coupled movements, and the later works indicate an influence on precipitates.

Based on these works, the present paper aims to establish a quantitative link between shear-coupled grain boundary relaxation and (coherent) precipitation from a thermomechanical perspective. It turns out that this combination can locally alter

the thermodynamic landscape and therefore favor precipitation near grain boundaries, in agreement with the observations mentioned above. To concisely demonstrate the concept of the interaction between shear-coupled grain boundaries and precipitates, we follow the perturbation analysis published in Ref. [19]. Spherical precipitates are introduced in the vicinity of the grain boundary, and the correlation between the elastic fields is investigated. The interaction between precipitates and a grain boundary leads to an elastic interaction term, which allows the system to lower its elastic free energy. It can therefore be favorable for precipitates to be located at specific locations near a shear-coupled grain boundary. The consequence is a solubility limit change at these positions.

This paper is structured as follows. After a brief discussion of shear-coupled motion in Sec. II, we derive the elastic energy of an independent shear-coupled grain boundary and isolated precipitates in Sec. III. In Sec. III C the interaction is considered, leading to correlation terms. The interaction terms potentially lower the free elastic energy of the system. This induces a grain boundary shape change as a result of the energy minimization, as discussed in Sec. IV. Moreover, this leads to a solubility limit change and therefore a local modification of phase diagrams for alloys, which is discussed in Sec. V.

II. SHEAR-COUPLED MOTION

A general law of grain boundary motion caused by shear stress is given in Ref. [9], describing the tangential grain velocity $v_{||}$ as

$$v_{||} = S\tau + \beta v_n. \tag{1}$$

The tangential sliding velocity is thus a resulting combination of sliding and normal grain boundary motion v_n. The first term on the right side describes the sliding motion of a grain due to a shear stress τ acting at the top grain by a sliding coefficient S. The second term captures the coupling to the normal grain boundary velocity v_n via the coupling factor β. A sketch to illustrate the two mechanisms is shown in Fig. 1. In this work we focus on the case of pure shear-coupled motion, therefore using the relation

$$v_{||} = \beta v_n. \tag{2}$$

For symmetric [001] tilt grain boundaries, the coupling factor is dependent on only the crystallographic landscape if the temperature is well below the melting temperature, $T < 0.7\ T_M$, as shown in Ref. [9]. This grain boundary behavior is applicable for low- and high-angle tilt boundaries [8–10]. For low misorientation angles near zero ($\theta \to 0$) one uses

$$\beta_{\langle 100\rangle} = 2\tan\left(\frac{\theta}{2}\right). \tag{3}$$

This relation changes to a second branch for misorientation angles approaching the opposite limit, $\theta \to 90^\circ$, which leads to the relationship

$$\beta_{\langle 110\rangle} = -2\tan\left(\frac{\pi}{4} - \frac{\theta}{2}\right). \tag{4}$$

These two relations originate from two different slip directions of the grain boundary dislocations and can be derived using the Frank-Bilby equation [10]. The transition angle at which the coupling factor changes from the $\langle 100\rangle$ mode to the $\langle 110\rangle$ mode is dependent on temperature, as reported in Ref. [9] for copper. For aluminum, the coupling factor is independent of temperature and remains in the $\langle 100\rangle$ mode at high misorientation angles, according to MD simulations [20]. The coupling factor β has been analyzed and confirmed multiple times via experiments [21,22] and simulations [23,24] for different materials and symmetric tilt boundaries.

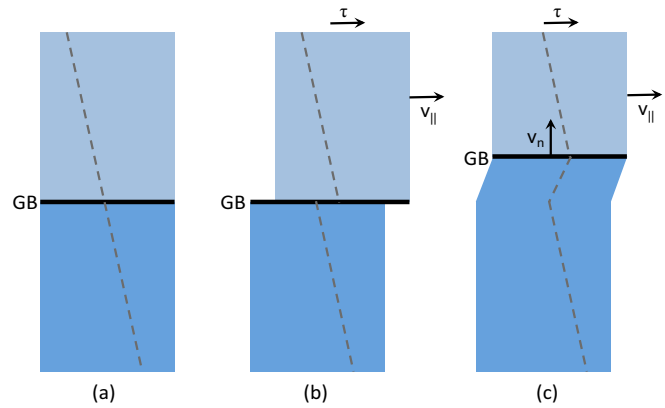

FIG. 1. (a) Illustration of sliding and shear-coupled grain boundary motion for a horizontal grain boundary (GB) as shown in the reference state. The upper grain is sheared by a stress τ, which leads to a tangential velocity $v_{||}$. (b) For pure sliding, the grain boundary maintains its position, whereas (c) for shear-coupling, grain boundary normal motion with velocity v_n occurs.

III. ELASTIC ENERGY

For simplicity, we investigate a two-dimensional setup, which contains a grain boundary and circular (cylindrical in three dimensions) precipitates; see Fig. 2 for a sketch. The grain boundary is allowed to undergo shear-coupled motion, while the coherent precipitates of radius R are located in the surrounding matrix above or below the grain boundary. The precipitates are assumed to have an isotropic elastic lattice mismatch (eigenstrain ε_0) with the matrix phase, leading to the appearance of coherency stresses. A morphological perturbation of the grain boundary due to shear-coupled motion leads to an increase of elastic energy and to an interaction between the boundary and the precipitates. In order to analyze the

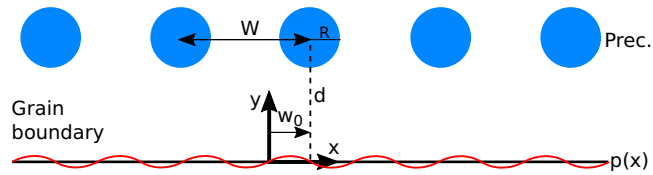

FIG. 2. Illustration of a (single-sine-mode) perturbation of the grain boundary via the function $p(x)$. Additionally, precipitates in an array with interval length W are located at a distance d on top of the grain boundary, measured by the line between $y = 0$ and the center of the precipitates. A horizontal shift of the precipitate array is defined by the parameter w_0; thus, the center of one precipitate is located at $x = w_0$.

described problem, we follow the approach of Karma *et al.* [19]. We use linear isotropic elasticity where the elastic constants of the matrix phase and the precipitates are assumed to be equal. The approach involves the derivation of displacement fields, the calculation of the free-elastic-energy density and, finally, an integration to yield the free elastic energy. The final result of the free elastic energy of the depicted setup will consist of three main parts, the elastic grain boundary energy, the elastic energy of the precipitates, and the interaction energy between the grain boundary and inclusions.

A. Grain boundary energy

An initially straight grain boundary, expressed by the function $y = 0$, is deformed by

$$p(x) = \sum_{k=0}^{\infty} [a(k)\cos(kx) + b(k)\sin(kx)], \tag{5}$$

where $a(k)$ and $b(k)$ are wave-number-dependent Fourier series amplitudes of the perturbation. In order to utilize this form of the perturbation, a periodic system has to be considered. Although we focus on an isolated grain boundary first, the periodicity constraint has the implication that the precipitates are arranged periodically as well. Their vertical positions are defined by the parameter d, the distance between the unperturbed grain boundary and the center of the precipitates, and W is the lateral spacing between them. This parameter defines the periodicity of our setup and therefore leads to a direct definition of the wave numbers used in the Fourier series,

$$k = \frac{2\pi m}{W}, \quad m = 0, 1, 2, \ldots. \tag{6}$$

The last free parameter is the shift of the precipitates in the horizontal direction, defined by w_0 (after energy minimization this parameter will drop out, reflecting the translational invariance of the problem). For $w_0 = 0$, one precipitate is located symmetrically above $x = 0$. The deformation of the grain boundary via the function $p(x)$ in the context of shear coupling not only is a movement in the normal direction but also implies a tangential displacement of the grains. The central boundary condition of the elastic problem reflects the shear-coupled motion relation, Eq. (2), by expressing the lateral displacement via [19]

$$u_x^+(x, 0) - u_x^-(x, 0) = \beta p(x) \tag{7}$$

up to linear order in $p(x)$, which serves as an expansion parameter. Here, one has to distinguish between the displacement components in the upper (u_i^+, $y > 0$) and lower (u_i^-, $y < 0$) domains. The energy density is given by

$$f = \tfrac{1}{2}\lambda\varepsilon_{kk}^2 + \mu\varepsilon_{ij}^2 \tag{8}$$

in terms of the strain tensor $\varepsilon_{ij} = (\partial_j u_i + \partial_i u_j)/2$, using the shear modulus μ and the Lamé coefficient $\lambda = 2\mu\nu/(1 - 2\nu)$ with the Poisson ratio ν. The elastic free energy is obtained by integration of the elastic energy density. In the horizontal direction the integration is determined by the periodic length unit $L = NW$,

$$F^{\mathrm{GB}} = \int_0^L dx \int_{-\infty}^{\infty} dy\, f(u_x, u_y), \tag{9}$$

with N being the number of precipitates. Details of the integration are shown in the Supplemental Material [25]; the final result for an isolated grain boundary without precipitates reads

$$F^{\mathrm{GB}} = \sum_{k=0}^{\infty} \left(\frac{\mu W N}{8(1-\nu)} \beta^2 k a^2(k) + \frac{\mu W N}{8(1-\nu)} \beta^2 k b^2(k) \right), \tag{10}$$

which corresponds to the result presented in Ref. [19] for a single cosine mode.

B. Energy of precipitates

We assume that the precipitates have a purely dilatational or compressive isotropic eigenstrain ε_0 with respect to the mother phase (hence, the equilibrium strain in a stress-free precipitate phase would be $\varepsilon_{ij} = \varepsilon_0 \delta_{ij}$).

The bulk free elastic energy of the two-phase system with a coherent interface between the matrix and precipitate of radius R is, according to the Bitter-Crum theorem [26],

$$F^{\mathrm{prec}} = \pi R^2 \varepsilon_0^2 \frac{E}{(1-\nu)}, \tag{11}$$

with E being Young's modulus, which is related to the previous elastic parameters via $E = 2\mu(1 + \nu)$. The elastic energy depends only on the total volume/area of the precipitate and not on the geometric arrangement. For the considered case of vanishing elastic constant contrast between the phases and isotropic elasticity and eigenstrain, multiple precipitates do not interact in the bulk. Therefore, N of them lead to an increase of elastic energy by the factor N (provided that they do not overlap, $R < W/2$),

$$F^{\mathrm{prec}} = N\pi R^2 \varepsilon_0^2 \frac{E}{(1-\nu)}. \tag{12}$$

C. Interaction and total elastic energy

The grain boundary modes and the precipitates have been considered separately up to this point. Due to linearity, the total displacement, strain, and stress fields are the sum of the contributions from the grain boundary and the precipitates. Since the elastic energy is quadratic in strain, a cross term between the two contribution emerges, in addition to the contributions (10) and (12). The integration of the cross-term energy density has been performed by a numerical integration method. By changing the modeling parameters on multiple scales, a reliable closed expression for the interaction energy has been determined, which reads [25]

$$F^{\mathrm{int}} = \frac{\Pi}{2} \frac{E}{1-\nu} \varepsilon_0 \beta R^2 N \sum_{k=0}^{\infty} \exp(-kd) k [a(k)\sin(kw_0) - b(k)\cos(kw_0)]. \tag{13}$$

This expression is valid for precipitates which are located in the upper grain, $y > 0$, and which do not intersect with the grain boundary, $d > R$. Similarly, precipitates in the lower

grain lead to the same expression with opposite sign. The parameter Π in Eq. (13) is a constant which is approximately π but deliberately left uncertain due to potential minor numerical inaccuracies. In the following we will assume $\Pi = \pi$.

The total elastic free energy of the system with an infinite number of grain boundary perturbations and N precipitates is given as the sum of all contributions,

$$F = F^{\mathrm{prec}} + F^{\mathrm{GB}} + F^{\mathrm{int}}. \tag{14}$$

IV. INTERPRETATION

A. Energy minimization

Inspection of the interaction energy (13) shows that the energy can be either increased or decreased, leading to a repulsive or attractive interaction for a fixed grain boundary shape $p(x)$. This becomes obvious from the fact that both the eigenstrain ε_0 and the shear-coupling factor β can be either positive or negative. The eigenstrain depends on the relative volume change of the precipitate in comparison to the matrix, while the coupling factor follows directly from Eqs. (3) and (4).

The main unique aspect emerges from the fact that if shear-coupled rearrangements of the grain boundary are possible, it can arrange such that the total free energy is minimized. For illustrational purposes we follow this under the assumption that the energy contributions in Eq. (14) are dominant; hence, we suppress higher-order corrections of the grain boundary energy F^{GB} from the perspective of the perturbative approach with small shape deviations $p(x)$ and also assume that a bare grain boundary energy, which depends on the grain boundary length, is subdominant to the elastic energy contributions which arise from the shear coupling. Then, energy minimization with respect to the Fourier amplitudes $a(k), b(k)$ gives [25]

$$F^{\mathrm{min}} = F^{\mathrm{prec}}\left(1 - \frac{\pi^2(1+\nu)}{2}\frac{R^2}{W^2 \sinh^2\left(\frac{2\pi d}{W}\right)}\right). \tag{15}$$

Obviously, this energy is lower than the precipitates' energy near planar grain boundaries ($F^{\mathrm{GB}} = 0$); hence, a short-range attractive interaction with an exponential asymptotic decay emerges. This implies that the precipitate formation should occur more likely in the vicinity of the grain boundary.

An interesting outcome of this energy description is that the shear-coupling factor β drops out. The misorientation angle of the grain boundary no longer influences the energy, and therefore, the behavior is expected to be generic for a wide range of grain boundaries. Due to the energy minimization the lateral shift w_0 cancels, which means that the "phase" of the perturbations aligns properly to the location of the precipitates, as will be discussed in more detail in the following section. As the eigenstrain ε_0 appears quadratically in the energy expression, the attraction of the precipitates to the grain boundary is independent of the sign of the lattice mismatch.

In Fig. 3, the dimensionless free elastic energy $F_d^{\mathrm{min}} = F^{\mathrm{min}}/F^{\mathrm{prec}}$ dependent on d/W (the grain-boundary-precipitate to interprecipitate distance ratio) is shown. It expresses the reduction of elastic energy when the precipitates approach the shear-coupled grain boundary. In contrast, when F_d^{min} becomes unity for large separations, the interaction of inclusions and interface is negligible. Different ratios of

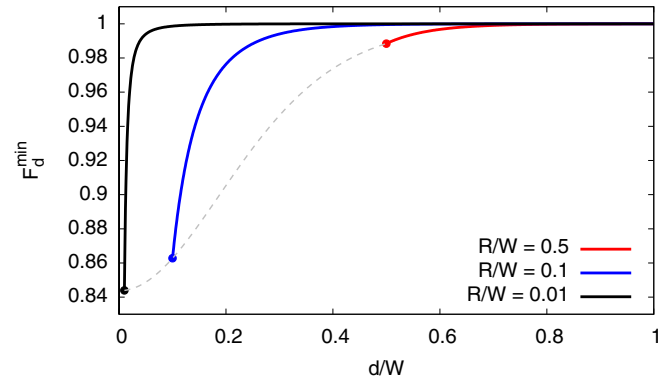

FIG. 3. Dimensionless free elastic energy $F_d^{\mathrm{min}} = F^{\mathrm{min}}/F^{\mathrm{prec}}$ as a function of the (dimensionless) precipitate distance to the grain boundary d/W for $\nu = 1/4$. Different combinations of R/W are chosen to illustrate the energy reduction dependent on the precipitate radius R. The curves start at positions indicated by dots, which reflect the condition $d \geqslant R$, such that the precipitates do not intersect with the grain boundary. The limit of this condition, $d = R$, is shown by the dashed curve.

R/W are used to illustrate the scaling of the free elastic energy with the precipitates' radius. The curves start at positions indicated by dots, marking the condition $d \geqslant R$, as, otherwise, the precipitates would intersect with the interface. We have confirmed numerically that such an intersection is energetically unfavorable. It is immediately visible that the precipitates favor small distances to the grain boundary (attractive interaction). On the other hand, when the precipitate radius R increases, the curves are shifted to the right, and the minimum value of F_d^{min} becomes larger. The system therefore favors small precipitates, as they can be closer to the grain boundary. Similarly, an increasing horizontal distance W between the precipitates is favorable, which expresses an effective mutual repulsion of the precipitates near the grain boundary.

B. Change of the grain boundary shape

From the optimized Fourier coefficients $a(k)$ and $b(k)$ the energetically favorable grain boundary contour is obtained from Eq. (5), which leads to [25]

$$p(x) = -\frac{\pi\varepsilon_0 R^2 4(1+\nu)}{W\beta} \times \frac{\exp\left(-\frac{2\pi d}{W}\right)\sin\left(\frac{2\pi(w_0-x)}{W}\right)}{1 - 2\exp\left(-\frac{2\pi d}{W}\right)\cos\left(\frac{2\pi(w_0-x)}{W}\right) + \exp\left(-\frac{4\pi d}{W}\right)}. \tag{16}$$

The result is demonstrated in Fig. 4 for different distances between precipitates and the grain boundary. Obviously, a straight interface is favorable for remote precipitates, and grain boundary perturbations become more pronounced for nearby inclusions.

An interesting feature is that the precipitates are not located at symmetry positions of the grain boundary, but rather on the left side of the perturbation maxima. This symmetry breaking emerges from a combination of the shear coupling

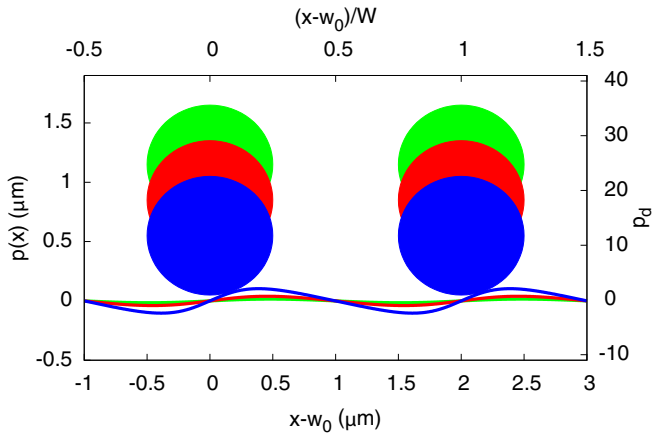

FIG. 4. Grain boundary shapes $p(x)$ for three different distances between the precipitates and the grain boundary, namely, $d_{\text{blue}} = 5.5\times10^{-7}$ m, $d_{\text{red}} = 8.5\times10^{-7}$ m, and $d_{\text{green}} = 1.15\times10^{-6}$ m. The parameters are $E = 175$ GPa, $\nu = 0.25$, $R = 5\times10^{-7}$ m, $W = 2\times10^{-6}$ m, $\beta = 0.07$, and $\varepsilon_0 = 0.02$. Corresponding dimensionless values are shown on the secondary axis.

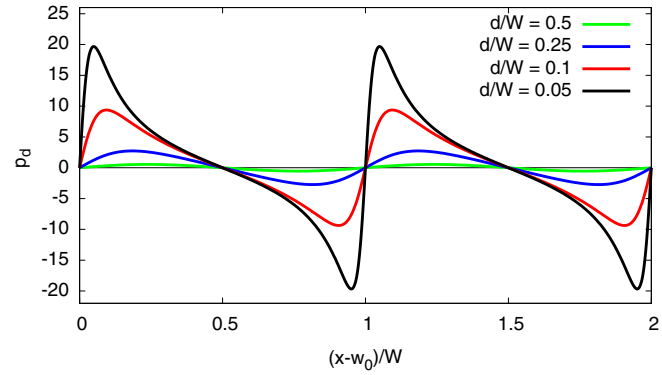

FIG. 5. The grain boundary shape equation (16) in its dimensionless form, $p_d(x/W) = p(x/W)(W\beta)/[\varepsilon_0 R^2(1+\nu)]$. Different values of d/W are used to show the effect of these two parameters on the grain boundary deformation.

and the dilatational eigenstrain of the precipitate. For $\varepsilon_0 > 0$ the surrounding matrix phase around a precipitate is compressed. Integration of the shear-coupling relation (2) gives the displacement mismatch $\Delta u_x = \beta p(x)$, which leads to compressive regions according to $\Delta\varepsilon_{xx} = \beta p'(x)$ for regions with positive slope $p'(x)$ and $\beta > 0$, in agreement with the optimized precipitate locations in Fig. 4.

The lateral offset w_0 appears only in the combination $x - w_0$, reflecting the translational invariance of the problem.

Both the precipitate shape and the elastic free energy have a quadratic dependence on the precipitate radius R. The deformation of the grain boundary therefore increases with the radius, once again constrained by the condition $d \geqslant R$, such that a crossing of the grain boundary does not occur. The initial state of the grain boundary is naturally recovered when the radius vanishes ($R = 0$), correctly showing that the grain boundary recovers its shape of a straight line if no precipitates are present.

To get a deeper understanding of the functional dependencies of the equilibrium grain boundary contour on the other length scales we show it in dimensionless form, $p_d(x/W) = p(x/W)W\beta/[\varepsilon_0 R^2(1+\nu)]$, in Fig. 5 for different distance ratios d/W. It is clear that the magnitude of the grain boundary deformation increases when W increases. In extreme cases, when W becomes large, the denominator of Eq. (16) can become singular, as the exponential functions reach unity. In this case, the precipitates are far away from each other, such that they can be characterized as independent inclusions. The result of this extreme case can be interpreted as a breakup of the grain boundary at the locations of the precipitates at w_0. This outcome is in agreement with phase field crystal simulation results [18], for which it has been demonstrated that a single precipitate can lead to the breakup of a shear-coupled grain boundary. We note that in between remote precipitates the grain boundary slope scales as $p'(x = w_0 + W/2) \sim 1/W^2$; hence, the grain boundary remains essentially flat there.

V. SOLUBILITY LIMIT CHANGES DUE TO SHEAR-COUPLED MOTION

To understand the influence of shear-coupled motion on phase separation, the total Gibbs energy including thermochemical contributions next to the elastic energy has to be considered. Similar to the analysis in Ref. [3], where phase separation with an elastic mismatch in the vicinity of free surfaces has been studied, we focus on binary alloys with coexistence between a disordered solid-solution α phase with zero solubility at $T = 0$ K and another β phase with coexistence concentration $c_{\beta,0}$ at $T = 0$ K; see Fig. 6 for a sketch of the phase diagram. We assume the α phase is dominated by the configurational entropy contribution (per particle) $g_c \simeq kTc\ln(c/c_0)$ to the Gibbs energy for low solute concentrations $c \ll 1$ and low absolute temperature T. From the asymptotic consideration of the stress-free common tangent

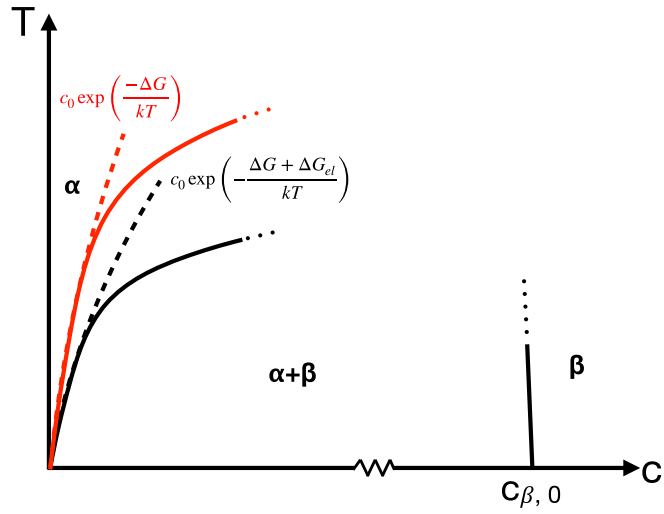

FIG. 6. Sketch of the phase diagram. The solubility limit without consideration of elastic effects is shown in red; elastic bulk effects are in black. The dashed curves are the Arrhenius approximations according to Eqs. (17) and (18) for the low-temperature limit. The (local) phase diagram near shear-coupled grain boundaries lies in between the red and black curves.

construction the solubility limit of the α phase is given by an Arrhenius expression (k is the Boltzmann constant),

$$c_\alpha(T) = c_0 \exp(-\Delta G/kT), \tag{17}$$

with the formation enthalpy difference ΔG, which contains the energetic balance between phases α and β (see Ref. [3] for a detailed discussion). The inclusion of elastic coherency bulk effects leads—for the same assumptions as in the present work, i.e., isotropy, dilatational mismatch, and vanishing contrast between the elastic constants between the phases—to a shift of the formation enthalpy difference according to

$$\Delta G \to \Delta G + \Delta G_{\mathrm{el}} = \Delta G - \frac{E}{1-\nu}\frac{\varepsilon_0^2}{c_{\beta,0}}\Omega_\alpha, \tag{18}$$

with the atomic volume Ω_α of the pure α phase. Consequently, the bulk solubility limit of the α phase is therefore increased in comparison to the stress-free case. The central outcome of Ref. [3] is that near free surfaces elastic stresses can partially relax and therefore attenuate the elastic energy contribution in Eq. (18) by a dimensionless factor $1-\gamma$, i.e.,

$$\Delta G \to \Delta G + (1-\gamma)\Delta G_{\mathrm{el}}. \tag{19}$$

The parameter γ has been calculated for a variety of configurations, and for stress relaxation, $0 < 1-\gamma < 1$, the solubility limit of the α phase is therefore decreased in comparison to the bulk coherent phase diagram. This effect promotes precipitate formation near free surfaces, as expressed through the solubility modification factor [3]

$$s = \frac{c_\alpha^{\mathrm{surface}}(T)}{c_\alpha^{\mathrm{bulk}}(T)} = \exp\left(\frac{\gamma\,\Delta G_{\mathrm{el}}}{kT}\right). \tag{20}$$

A similar effect can now be expected for phase separation near shear-coupled grain boundaries, which substantiates an earlier effective description [4]. This morphological degree of freedom allows us to reduce the elastic energy when a precipitate forms near the grain boundary, as discussed in the preceding sections. Here, we readily get from Eq. (15)

$$1-\gamma = \frac{F^{\min}}{F^{\mathrm{prec}}} = 1 - \frac{(1+\nu)\pi^2 R^2}{2W^2}\frac{1}{\sinh^2\left(\frac{2\pi d}{W}\right)}, \tag{21}$$

which is obviously stress relieving, $1-\gamma < 1$, and therefore reduces the solubility limit of the α phase against β precipitate formation near shear-coupled grain boundaries. Expression (21) coincides with the dimensionless elastic energy shown in Fig. 3, which shows that a noticeable reduction of the order of 10% of the elastic energy is possible. Remarkably, the result (21) depends neither on the value of the eigenstrain of the precipitate phase nor on the shear-coupling factor but mainly on the locations of the precipitates. Additionally, one can observe that the radius still plays a vital role, which is again limited by the constraint $d \geqslant R$.

In order to estimate the influence of the shear-coupling effect on the local solubility limit change we apply the results to the iron-carbon system. For simplicity, we neglect corrections due to anisotropy and elastic constant contrasts, which lead to minor quantitative changes. Fe-C has a phase diagram of the investigated type for the bcc α ferrite-cementite (Fe_3C) coexistence for temperatures below about 1000 K. Whereas the ferrite is a solid-solution phase with carbon in octahedral interstitial positions, the cementite appears as a stoichiometric phase with a carbon concentration of $c_{\beta,0} = 1/3$ (which equals 6.67 wt%). Using as approximative parameters $T = 300$ K, $\varepsilon_0 = 0.0463$, $R = 0.1\,\mu$m, $W = 10\,\mu$m, $E = 175$ GPa, $\nu = 0.25$, $d = R$, and an atomic volume $\Omega_\alpha = 11.78\,\text{Å}^3$, one obtains a solubility modification factor of $s \approx 0.5$. Hence, carbides are expected to precipitate near shear-coupled grain boundaries already at carbon concentration of about half of the bulk solubility limit. This surprisingly large effect may have significant implications for the mechanical properties of the steels.

VI. SUMMARY AND CONCLUSIONS

Shear coupling of grain boundaries is a mechanism which can lead to mechanical stress relaxation. As a consequence, attractive interactions between other stress sources like precipitates can result. We have evaluated this effect in the framework of isotropic linear elasticity and coherent, spherical precipitation with a dilatational mismatch to demonstrate the concept. Small corrugations of the grain boundary provoke (positive) elastic energy due to shear coupling next to the bare (also positive) energy of an array of inclusions. An energetic cross term, however, can lower the total energy and therefore favor the formation of the precipitates near the grain boundary (attractive interaction). Energy minimization predicts the strength and range of this short-range interaction as well as the corresponding equilibrium grain boundary profile. A consequence is the local alteration of alloy thermodynamics with a reduced solubility limit near grain boundaries. Applying these findings to the iron-carbon system allows us to qualitatively estimate the effect of the grain boundary and precipitate interaction. The interstitial model shows that in the context of shear-coupled motion a correction of the solubility limit of about 50% at room temperature is possible.

The serration of grain boundaries in Ni-based superalloys [27–29] is a possible application of the present theory, as similarly argued by Xu *et al.* [18]. The formation of primary γ' particles during the heat treatment is mandatory for this phenomenon and is a common event in the manufacturing process. The particles are favored near grain boundaries, while the latter are deformed simultaneously. A correlation with primary γ' size and serration amplitude has been established, which is in agreement with our findings. The interaction of precipitates and grain boundaries was already attributed to elastic energy relaxation in Ref. [27] but requires the formation of precipitates at the grain boundary first. With the present concept of combined precipitation and shear-coupled motion one can potentially explain why γ' particles precipitate near the grain boundary with a simultaneous deformation of the grain boundary contour.

ACKNOWLEDGMENTS

This work was supported by the DFG via the priority program, Grant No. SPP 1713. The authors gratefully acknowledge the computing time granted on the supercomputer JURECA at the Jülich Supercomputing Centre (JSC).

[1] Y. J. Park and I. M. Bernstein, Metall. Trans. A **10**, 1653 (1979).
[2] A. J. Ardell, Metall. Trans. A **16**, 2131 (1985).
[3] R. Spatschek, G. Gobbi, C. Hüter, A. Chakrabarty, U. Aydin, S. Brinckmann, and J. Neugebauer, Phys. Rev. B **94**, 134106 (2016).
[4] M. Weikamp, C. Hüter, and R. Spatschek, Metals **8**, 219 (2018).
[5] W. T. Read and W. Shockley, Phys. Rev. **78**, 275 (1950).
[6] C. H. Li, E. H. Edwards, J. Washburn, and E. R. Parker, Acta Metall. **1**, 223 (1953).
[7] D. W. Bainbridge, H. L. Choh, and E. H. Edwards, Acta Metall. **2**, 322 (1954).
[8] J. W. Cahn and J. E. Taylor, Acta Mater. **52**, 4887 (2004).
[9] J. W. Cahn, Y. Mishin, and A. Suzuki, Acta Mater. **54**, 1953 (2006).
[10] J. W. Cahn, Y. Mishin, and A. Suzuki, Philos. Mag. **86**, 1 (2006).
[11] A. Adland, A. Karma, R. Spatschek, D. Buta, and M. Asta, Phys. Rev. B **87**, 024110 (2013).
[12] D. A. Molodov, T. Gorkaya, and G. Gottstein, J. Mater. Sci. **46**, 4318 (2011).
[13] Z. T. Trautt, A. Adland, A. Karma, and Y. Mishin, Acta Mater. **60**, 6528 (2012).
[14] T. Gorkaya, K. D. Molodov, D. A. Molodov, and G. Gottstein, Acta Mater. **59**, 5674 (2011).
[15] K. Cheng, L. Zhang, C. Lu, and K. Tieu, Sci. Rep. **6**, 25427 (2016).
[16] L.-L. Niu, Y. Zhang, X. Shu, F. Gao, S. Jin, H.-B. Zhou, and G.-H. Lu, Sci. Rep. **6**, 23602 (2016).
[17] P.-A. Geslin, X. Yechuan, and A. Karma, Phys. Rev. Lett. **114**, 105501 (2015).
[18] Y. Xu, P.-A. Geslin, and A. Karma, Phys. Rev. B **94**, 144106 (2016).
[19] A. Karma, Z. T. Trautt, and Y. Mishin, Phys. Rev. Lett. **109**, 095501 (2012).
[20] V. A. Ivanov and Y. Mishin, Phys. Rev. B **78**, 064106 (2008).
[21] T. Gorkaya, D. Molodov, and G. Gottstein, Acta Mater. **57**, 5396 (2009).
[22] D. Molodov, V. A. Ivanov, and G. Gottstein, Acta Mater. **55**, 1843 (2007).
[23] E. R. Homer, S. M. Foiles, E. A. Holm, and D. L. Olmsted, Acta Mater. **61**, 1048 (2013).
[24] C. Hüter, J. Neugebauer, G. Boussinot, B. Svendsen, U. Prahl, and R. Spatschek, Continuum Mech. Thermodyn. **29**, 895 (2017).
[25] See Supplemental Material at http://link.aps.org/supplemental/10.1103/PhysRevB.100.054103 for details of the calculations.
[26] P. Fratzl, O. Penrose, and J. L. Lebowitz, J. Stat. Phys. **95**, 1429 (1999).
[27] A. K. Koul and G. H. Gessinger, Acta Metall. **31**, 1061 (1983).
[28] A. K. Koul and R. Thamburaj, Metall. Trans. A **16**, 17 (1985).
[29] R. J. Mitchell, H. Y. Li, and Z. W. Huang, J. Mater. Process. Technol. **209**, 1011 (2009).